Nonlinear dynamics of additive-pulse mode-locked lasers in four cavity topologies

U. Morgner and F. Mitschke
Institut für Angewandte Physik, Universität Münster, Corrensstrasse 2/4, D-48149 Münster, Germany
(Received 20 September 1996)

Coupled-cavity mode-locked lasers, useful as they may be, can have a tendency to display dynamic instabilities; the mechanisms for this phenomenon are poorly understood. We show here by analytic means, supplemented with numerics, how these instabilities arise from the coupling of nonlinear resonators and how the thresholds for instability depend strongly on the topology of the laser. Four different topologies are considered, the Michelson, the Fabry-Pérot, and two further configurations. The results of this comprehensive theory identify the most stable and the most unstable configuration and explain empirical findings of several authors. [S1050-2947(97)01204-3]

PACS number(s): 42.65.Sf, 42.65.Re, 42.60.Da, 42.60.Fc

INTRODUCTION

Coupled-cavity mode-locked lasers [1], also known as soliton lasers [2,3], interferentially mode-locked lasers [4,5], or additive-pulse mode-locked (''APM'') lasers [6–11], have been demonstrated to be useful tools for a variety of investigations. In most cases a single mode optical fiber is used as the nonlinear medium because this choice is both effective and economical. Since no specialized components are required, any lab in possession of a Nd:YAG laser could configure it as a source of ps pulses by adding just a few standard items. On the other hand, any system of coupled nonlinear resonators is likely to be prone to dynamical instabilities like period doubling and chaos. In fact, for APM lasers employing an optical fiber as a nonlinear element, the ocurrence of such instability has been experimentally established [12,13]. Several authors have noted that the way in which the cavities are connected (in other words the cavity topology) has an influence on the stability of the system [6,14–16]. There are indications that this is not a mere technical difference but rather deeply rooted in the dynamics of the system [16]. Unfortunately, so far theoretical guidance has been lacking on this matter.

By studying this class of lasers, we try to obtain further insight into the behavior of coupled nonlinear oscillators for both fundamental and practical reasons. We present analytical models for four possible cavity arrangements. The Fabry-Pérot and Michelson geometries have been considered by several authors before. We extend our approach to the ''P'' and ''Q'' configurations mentioned by [17]; note that we prefer to call the latter the ''Φ'' configuration. We begin by formulating maps for each topology within the framework of a quasicontinuous-wave (CW) treatment. For the limitations of this treatment, see below.

I. QUASI-CW MODEL

Since we deal here with nonlinear, i.e., power-dependent effects, some value of power must be inserted in the equations to be derived below. This is straightforward in the case of constant power; however, we are concerned mainly with pulses of light which by definition have a temporally varying power. We will proceed as follows: To keep the mathematics manageable, we will consider sufficiently narrow ''time slots,'' or slices, from the pulse and treat them as if they evolved in independence from neighboring slices. Formally, we can then proceed as in the cw treatment of Ikeda [18,19]. We call this simplification the ''quasi-cw'' approximation; it has been used in the context of passive fiber resonators by several authors [20,21]. In the end, we will return to the effect of the interaction between slices and argue that the threshold values for instabilities (our central result) are not affected.

For definiteness and graphical illustration, assume a laser pulse $P(t)=P_0\mathrm{sech}^2(1.76t/\tau)$ with the full width at half maximum (FWHM) τ. Split it up into several temporal slices of some width ΔT with powers P_i, where $P_{i=0}$ is at the pulse peak (see Fig. 1).

The quasi-cw laser model describes the interaction of one such slice with the gain medium and the fiber nonlinearity, according to rules set qualitatively by the topology and quantitatively by the splitting ratio of the beam splitter. The ''fast'' components—splitter and nonlinear phase shift—can be included in a straightforward manner. On the other hand, gain is ''slow'' in the sense that it depends on the energy of the whole pulse; within the framework of the quasi-cw approximation, we still have to include some global information on the remainder of the pulse. To this end we note that the pulse energy is given by

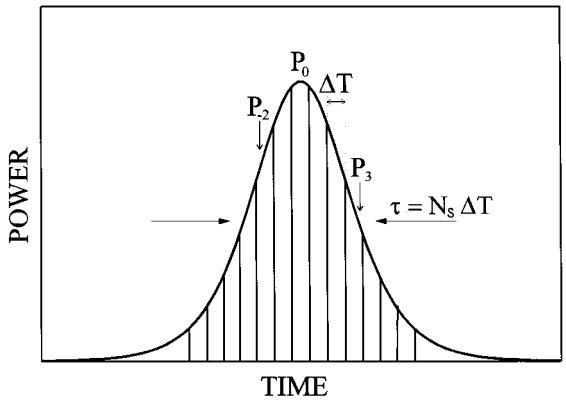

FIG. 1. Separation of the pulse into several slices P_i of width ΔT. N_s describes the number of slices in the pulse width τ.

$$W=\int P(t)dt=\Delta T\sum_{i=-\infty}^{\infty}P_i\approx P_0\tau \tag{1}$$

and the number of slices N_s in the pulse width is of the order of $N_s=\tau/\Delta T$. The energy contained in slice ''i'' is W_i and represents the fraction κ_i of the total energy, with

$$\kappa_i=\frac{W_i}{W}=\frac{P_i\Delta T}{P_0\tau}=\frac{1}{N_s}\mathrm{sech}^2\left(1.76\frac{i}{N_s}\right). \tag{2}$$

II. APM COMPONENTS

A. Gain medium

We are mainly concerned here with solid-state lasers which have a very small emission cross section. It is therefore a reasonable approximation to neglect dynamical contributions to gain saturation. The power gain $G(W)$ of a double pass through the laser medium as a function of the intracavity pulse energy W is then written as [22]

$$\overline{G(W)}=\exp\left(\frac{g_0}{1+W/W_s}\right), \tag{3}$$

with g_0 the small signal gain of a double pass and W_s the saturation energy. g_0 can be measured from the relaxation oscillation frequency [23]. We use here values as measured for our Nd:YAG laser, namely, $g_0=0.7$ and $W_s=130$ nJ.

Estimating the energy W of the whole pulse from the power of the slice with index i we arrive at the power gain

$$G(P_i)=g^2(P_i)=\overline{G}(\Delta TP_i/\kappa_i), \tag{4}$$

$$=\overline{G}\left(\frac{P_i\tau}{\mathrm{sech}^2(1.76i/N_s)}\right), \tag{5}$$

where $g(P_i)$ is the field amplitude gain. We assume here a pulse width of $\tau=10$ ps. Obviously, the slice with $i=0$ is the most interesting; all results given below will refer to this slice.

B. Beam splitter

We will use the following convention for the notation of properties of the beam splitter: Reflectivities are denoted by the letter R or r, and transmissivities by the letter T or t, where upper case refers to power and lower case to field amplitude. The relation $R=r^2=1-T=1-t^2$ is understood (lossless beam splitter).

At the beam splitter, two incident complex field amplitudes a_1,a_2 interfere. The resulting amplitudes b_1,b_2 are given as [24]

$$b_1=ra_1+ta_2, \tag{6}$$

$$b_2=ta_1-ra_2, \tag{7}$$

where the negative sign in Eq. (7) refers to the phase jump of π due to the reflection at the medium of higher refractive index.

C. Fiber nonlinearity

The optical Kerr effect in monomode fibers leads to an intensity-dependent refractive index n according to

$$n=n_0+n_2P/A_{\mathrm{eff}}, \tag{8}$$

where n_0 is the classical, or small-signal, index, n_2 the nonlinearity coefficient, and A_{eff} the modal cross section. The resulting self-phase modulation in a fiber of length L leads to a nonlinear phase shift $\varphi_{\mathrm{nl}}(t)$ given by [25]

$$\varphi_{\mathrm{nl}}=\frac{2\pi n_2}{\lambda A_{\mathrm{eff}}}LP=\gamma LP \tag{9}$$

(λ is the wavelength).

III. JACOBIAN AND LYAPUNOV EXPONENTS OF MAPS

A useful tool to describe the dynamical behavior of a map quantitatively is the use of Lyapunov exponents. Their number corresponds to the dimension of phase space. Their real parts describe the stability against small perturbations; a system is stationary if all real parts are smaller than zero. (The existence of at least one exponent with positive real part has been used as a definition for a chaotic system [26].)

For an N-dimensional map

$$\vec{x}^{(n+1)}=\vec{f}(\vec{x}^{(n)}) \tag{10}$$

the Jacobian (or Floquet matrix) J is defined as

$$J^{(n)}:=\begin{pmatrix}\left.\frac{\partial f_1(\vec{x})}{\partial x_1}\right|_{\vec{x}^{(n)}} & \cdots & \left.\frac{\partial f_1(\vec{x})}{\partial x_N}\right|_{\vec{x}^{(n)}}\\ \vdots & & \vdots\\ \left.\frac{\partial f_N(\vec{x})}{\partial x_1}\right|_{\vec{x}^{(n)}} & \cdots & \left.\frac{\partial f_N(\vec{x})}{\partial x_N}\right|_{\vec{x}^{(n)}}\end{pmatrix}, \tag{11}$$

and the Lyapunov multipliers $\vec{\Lambda}$ as [27]

$$\vec{\Lambda}=\lim_{n\to\infty}\left|\mathrm{EV}(J^{(n)}J^{(n-1)}\cdots J^{(0)})\right|^{1/n}, \tag{12}$$

with $\vec{x}^{(n)}$ a sequence generated by the map Eq. (10), and $\mathrm{EV}(J)$ the eigenvalues. In practice Eq. (12) is computed by

$$\vec{\Lambda}\approx\left[\prod_{k=1}^{N_2}\left|\mathrm{EV}(J^{(kN_1-1)}\cdots J^{(kN_1-N_1)})\right|^{1/N_1}\right]^{1/N_2}, \tag{13}$$

where N_1 describes the number of matrices to multiply, and N_2 the number of eigenvalues to average. Without loss of generality, we enumerate the multipliers as

$$\Lambda_1\leqslant\Lambda_2\leqslant\cdots\leqslant\Lambda_N. \tag{14}$$

We find that Λ_1 can be calculated with high precision using the standard floating point unit on a digital computer with $N_1\approx100$ in a straightforward manner. Let us remark that due to small inaccuracies in the calculation of the eigenvectors, the estimators for all other multipliers converge to Λ_1 after a

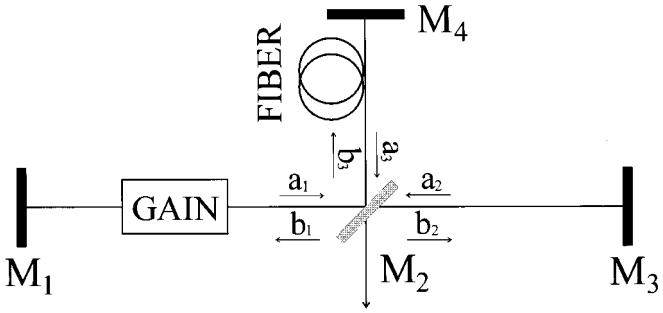

FIG. 2. The Michelson configuration. a_i, b_i denote field amplitudes; M_2 is the beam splitter.

few tens of matrix multiplications. Still, we could determine Λ_N with the same high precision by using the time inverted system

$$\Lambda_N^{-1}=\limsup_{n\to\infty}|\mathrm{EV}(J^{[-1](n)}\cdots J^{[-1](0)})|^{1/n}. \tag{15}$$

Λ_j with $j=2,\ldots,N-1$ could only be obtained with reduced precision using $N_1\approx 10$. However, since Λ_1 is the most relevant multiplier anyway for our purposes here, no further attempts were made to increase the precision on the intermediate multipliers. The Lyapunov exponents $\vec{\lambda}$ are then defined as

$$\lambda_j=\ln|\Lambda_j|,\quad j=1,\ldots,N. \tag{16}$$

In a one-dimensional system the Jacobian J is a scalar and equal to its eigenvalue. A fixed point of the map with $|J|<1$ is attractive and thus stable, whereas a fixed point with $|J|>1$ is repulsive and thus unstable. $J<-1$ is a necessary condition for the system to reach a two cycle, and possibly the beginning of a period-doubling sequence, quasiperiodicity, or chaos. We call such a fixed point a *dynamical fixed point*.

IV. APM CAVITY TOPOLOGIES

In most published studies [1–3,7–13] APM lasers were configured in the Fabry-Pérot (''FP'') topology. In several cases, however, a Michelson (''M'') topology was used with good success [4–6,14,15]. Meanwhile, some additional configurations have been realized [17,28]. Note that some seemingly different arrangements turn out to be topologically equivalent so that the total number of possible configurations is limited. For example, a figure-8 laser with two unidirectional rings is equivalent to the FP configuration. While some authors concluded that the M configuration is superior to the FP in terms of stability, it is not entirely clear yet which configuration is best for which purpose. We therefore discuss, one by one, all four topologies mentioned above.

A. The Michelson configuration

Consider a resonator formed by two highly reflecting (HR) mirrors M_1 and M_3, containing a gain medium and a partial reflector as a beam splitter M_2. The latter splits the light from the gain medium between the fiber branch and the air branch (see Fig. 2). The quantities a_i and b_i in Fig. 2 refer to complex field amplitudes; for the sake of clarity in the equations below we use the shorthand notation $P:=|p|^2$, where $p:=a_1$. The beam steered towards the fiber carries the power $|b_3|^2=PR$. A finite coupling efficiency from a free space propagating beam into a fiber is taken into account by $\eta<1$. The fiber is terminated at the distal end with a perfect reflection at mirror M_4. Thus the power $\eta^2|b_3|^2$ reenters the main cavity at the beam splitter. The reentrant light interferes with the light in the main cavity. The optical path length M_2–M_3 matches the length M_2–M_4 of the fiber branch, except for a tiny difference expressed as a phase offset φ_{stat}. In the fiber, self-phase modulation produces a nonlinear phase shift

$$\varphi_{\mathrm{nl}}=2\gamma LR\eta P. \tag{17}$$

The time evolution of a continuous laser field $p^{(n)}$ after the nth cavity round trip is given by the Michelson map

$$p^{(n+1)}=g(P^{(n)})p^{(n)}[T+R\eta e^{i[\varphi_{\mathrm{nl}}(P^{(n)})+\varphi_{\mathrm{stat}}]}], \tag{18}$$

with the gain term and the characteristic two beam interference of the linear and the nonlinear branch. It has the stable solution

$$p^{(n)}=\sqrt{P_0}e^{in\kappa}. \tag{19}$$

We see that there is a fixed point of the power, P_0, while there is no fixed point for the field since the phase rotates with a velocity κ, determined by

$$\sin\kappa=R\eta g(P_0)\sin[\varphi_{\mathrm{nl}}(P_0)+\varphi_{\mathrm{stat}}]. \tag{20}$$

To find P_0, we can restrict ourselves to a consideration of the evolution of power. It follows from Eq. (18) that

$$\begin{aligned}P^{(n+1)}&=G(P^{(n)})\{T^2+R^2\eta^2+2\eta TR\\&\quad\times\cos[\varphi_{\mathrm{nl}}(P^{(n)})+\varphi_{\mathrm{stat}}]\}P^{(n)}\\&=:G(P^{(n)})R_{\mathrm{eff}}(P^{(n)})P^{(n)}=:F(P^{(n)})P^{(n)}.\end{aligned} \tag{21}$$

In the absence of nonlinearity ($\gamma=0$), this one-dimensional map has exactly one fixed point. If $2\gamma L$ exceeds some threshold, simultaneously two more fixed points appear. At even higher nonlinearities, more pairs of fixed points appear, and one gets a possibly large odd number of fixed points (see Fig. 3). The stability of each fixed point is determined by the pertinent Jacobian. For the map Eq. (21) the Jacobian at the fixed point P_0 with $F(P_0)=1$ is given by

$$J=1+P_0\left.\frac{\partial F(P)}{\partial P}\right|_{P_0}. \tag{22}$$

One finds that the fixed points are alternately stable and unstable. From any of the stable fixed points a period-doubling scenario may occur, provided other parameters are adjusted such that J becomes smaller than $J=-1$. Thus the condition for the onset of instability is

$$\left.\frac{\partial F(P)}{\partial P}\right|_{P_0}=-2/P_0. \tag{23}$$

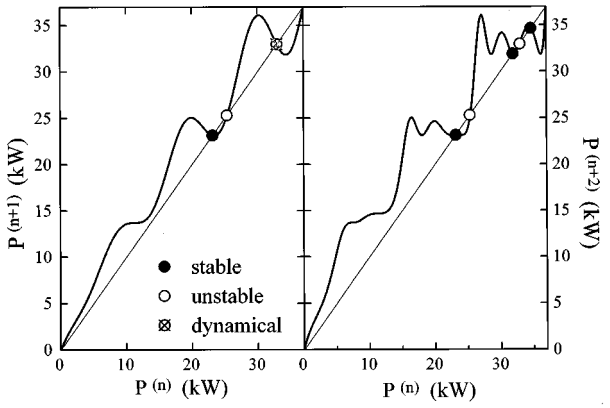

FIG. 3. Michelson map $P^{(n+1)}(P^{(n)})$ and its second iterate $P^{(n+2)}(P^{(n)})$. Parameters: $R=0.07$, $\eta^2=0.7$, $\gamma L=5\mathrm{kW}^{-1}$, and $\varphi_{\mathrm{stat}}=\pi/2$. One of the unstable fixed points is labeled as ''dynamical''; it generates two more stable fixed points in the second iterate indicative of a period doubling.

Figure 4 illustrates this condition. It shows the smallest nonlinear phase for which this condition can be satisfied as a function of the reflectivity of the beam splitter R, where the phase is obtained from power through Eq. (17). At large reflectivities the instability threshold tends to $\varphi_{\mathrm{nl}}\approx\pi$. For $R=0.12$ as used, e.g., in [14], the threshold is at about $\varphi_{\mathrm{nl}}=2.5\pi$, and at $R=0.05$ and below, the threshold rises to enormous nonlinear phase values.

It should be noted, however, that nonlinear phase shifts significantly larger than π cannot occur for a reason that is not included in this quasi-cw model: During start-up, some initially rather broad pulses will form; at this time the peak nonlinear phase shift $\hat{\varphi}_{\mathrm{nl}}$ will be much less than π. As the pulses then get shorter, $\hat{\varphi}_{\mathrm{nl}}$ will approach π. As soon as $\hat{\varphi}_{\mathrm{nl}}>\pi$, however, further pulse shortening ends. Indeed, in extensive numerical modeling we never encountered $\hat{\varphi}_{\mathrm{nl}}>1.6\pi$. Normal operation is thus expected at $\hat{\varphi}_{\mathrm{nl}}\approx\pi$, so that there is constructive interference at pulse peak, destructive interference in the far wings of the pulse, and no multiple pulsing.

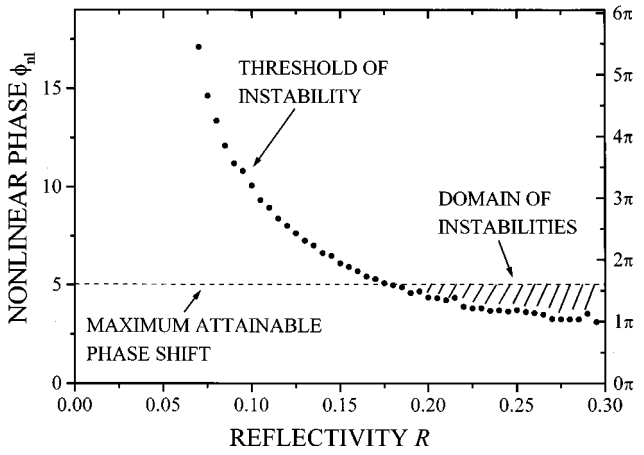

FIG. 4. Onset of instability as a function of coupling reflectivity R, ''M'' configuration. Parameters: $\eta^2=0.7$, φ_{stat} and γL were adjusted such that the minimum value of φ_{nl} resulted. The line at $\approx1.6\pi$ indicates the maximum possible nonlinear phase shift (see text).

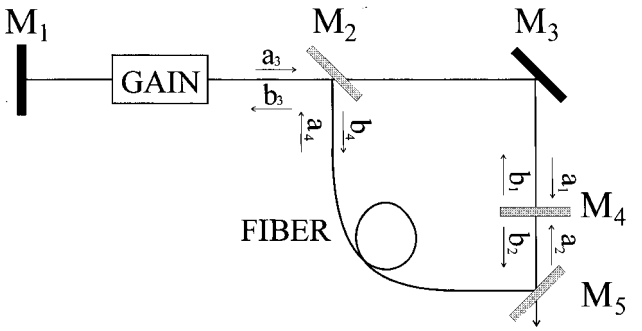

FIG. 5. The ''P'' configuration. a_i, b_i denote field amplitudes, M_2, M_4 are beam splitters, and M_5 is the output coupler.

This additional constraint is shown in Fig. 4 as a horizontal line at 1.6π. One sees that the threshold of instability in the ''M'' configuration can be reached only with coupling reflectivities larger than $R=0.16$. Only high gain laser media would be used with this substantial output coupling, and instabilities are unlikely to be a problem. We conclude that in an APM laser in Michelson topology with a reasonably low-beam-splitter reflectivity no dynamical instabilities can ever occur.

B. The ''P'' configuration

This configuration received its name due to its resemblance to the letter ''P.'' Since here we have to distinguish the reflectivity, etc., of several beam splitters and mirrors, we label the respective quantities with indices, as in Fig. 5. We assume $R_1=R_3=1$. Again the coupling efficiencies into and back from the fiber are η. The optical path lengths between M_2 and M_4 either via M_3 or via the fiber and M_5 are adjusted to be equal.

Similar to the ''M'' configuration this system can be described by a one-dimensional map: The temporal evolution of the laser field $p^{(n)}:=a_3^{(n)}$, $P:=|a_3|^2$ at the nth cavity round trip is given by

$$p^{(n+1)}=g(P)p^{(n)}[r_4(R_2R_5\eta^2e^{i(\varphi_{25}+\varphi_{52})}-T_2) - t_2t_4r_2r_5\eta(e^{i\varphi_{52}}+e^{i\varphi_{25}})]. \tag{24}$$

In this equation there are two nonlinear phase shifts, where

$$\varphi_{25}=\varphi_{\mathrm{stat}}+\gamma L\,\eta R_2P, \tag{25}$$

refers to the direction from M_2 towards M_5, and

$$\varphi_{52}=\varphi_{\mathrm{stat}}+\gamma LR_5\eta(T_2T_4+R_2R_4R_5\eta^2 - 2\eta r_2r_4r_5t_2t_4\cos\varphi_{25})P \tag{26}$$

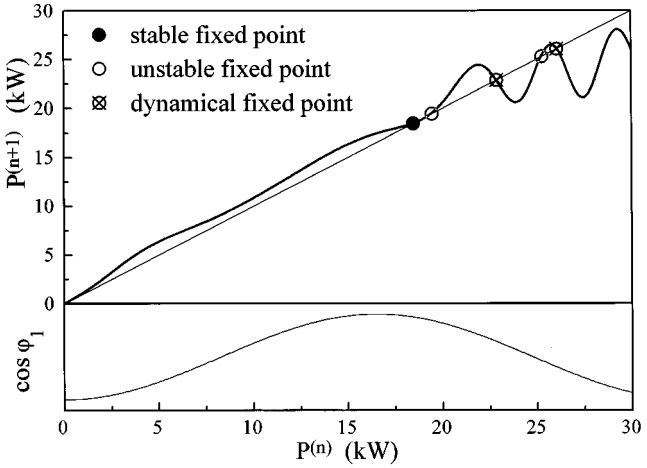

FIG. 6. ''P'' map $P^{(n+1)}(P^{(n)})$. Parameters: $R_2=0.04$, $R_4=0.8$, $\eta=0.7$, $R_5=0.6$, $\gamma L=6.8$ kW^{-1}, and $\varphi_{\rm stat}=\pi$. In the lower plot $\cos\varphi_{25}$ is shown.

refers to the opposite direction. Equation (24) leads to a map for the powers

$$\begin{aligned}P^{(n+1)}=&G(P^{(n)})\{[r_4(R_2R_5\eta^2\cos(\varphi_{25}+\varphi_{52})-T_2)\\&-t_2t_4r_2r_5\eta(\cos\varphi_{52}+\cos\varphi_{25})]^2\\&+[r_4R_2R_5\eta^2\sin(\varphi_{25}+\varphi_{52})\\&-t_2t_4r_2r_5\eta(\sin\varphi_{52}+\sin\varphi_{25})]^2\}P^{(n)}\\=&F(P^{(n)})P^{(n)}.\end{aligned}\tag{27}$$

Figure 6 shows the ''P'' map Eq. (27) (solid line). At small powers the graph follows the bisector closely; in this regime there is one attractive and one repulsive fixed point (= intersections with the bisector), indicated as filled and open circles, respectively. The first dynamical fixed point ($J<-1$) occurs at elevated powers, where the graph transits into undulations around the bisector. The undulations appear when $\cos\varphi_{25}(P)$ has negative slope and thus $d\varphi_{52}/dP$ is large.

The first dynamical fixed point (the one occurring at the lowest φ_{52}) is shown in Fig. 7 as a function of R_2. In comparison with Fig. 4, it is readily apparent that for the same nonlinear phase (i.e., power), the threshold of instability is reached at much smaller reflectivity. In conclusion we can say that although both ''M'' and ''P'' configurations can be described by one-dimensional maps, unstable output occurs at a considerably lower threshold for the ''P'' case, and should be observable experimentally.

C. The Fabry-Pérot configuration

This configuration has been the most popular until now; it is schematically shown in Fig. 8. The main resonator has an output coupler M_2; for notation of reflectivity, etc., see above. It is coupled to a fiber cavity of the same optical length except for a phase bias $\varphi_{\rm stat}$. With the optical-field amplitudes $p_i:=b_i$ and powers P_i in each cavity the nonlinear phase shift and the total phase are defined as

$$\varphi_{\rm nl}=2\gamma L\,\eta T_3P_2,\tag{28}$$

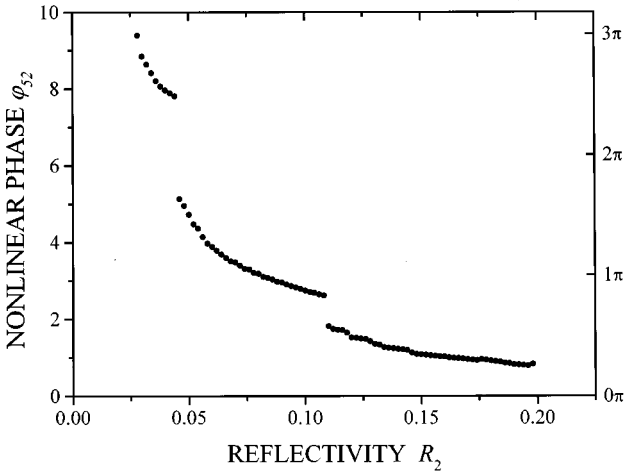

FIG. 7. Nonlinear phase shift at the first dynamical fixed point as a function of the coupling reflectivity R_2, ''P'' configuration. Parameters: $\eta=0.7$, $R_4=0.8$; $\varphi_{\rm stat}$, R_5, and γL were adjusted such that the minimum value of φ_{52} is obtained. The discontinuities in the curve are caused by transitions between the undulations of the map (see Fig. 6).

$$\varphi=\varphi_{\rm nl}+\varphi_{\rm stat}.\tag{29}$$

In our quasi-cw treatment we formulate the Fabry-Pérot map

$$\begin{aligned}p_1^{(n+1)}&=r_2g(P_1^{(n)})p_1^{(n)}+t_2\eta T_3e^{i\varphi}p_2^{(n)},\\p_2^{(n+1)}&=t_2g(P_1^{(n)})p_1^{(n)}-r_2\eta T_3e^{i\varphi}p_2^{(n)}.\end{aligned}\tag{30}$$

The corresponding expressions for the powers are

$$\begin{aligned}P_1=&R_2G(P_1)P_1+T_2\eta^2T_3^2P_2\\&+r_2t_2\eta T_3g(P_1)(p_1p_2^*e^{-i\varphi}+p_1^*p_2e^{i\varphi}),\end{aligned}\tag{31}$$

$$\begin{aligned}P_2=&T_2G(P_1)P_1+R_2\eta^2T_3^2P_2\\&-r_2t_2\eta T_3g(P_1)(p_1p_2^*e^{-i\varphi}+p_1^*p_2e^{i\varphi}).\end{aligned}$$

In contrast to the ''M'' and the ''P'' configurations this system is described by two coupled equations. This is related to the fact that energy can be stored in either cavity, so that there is a twofold memory effect. From Eqs. (31) we can derive the general relation between the two intracavity powers

$$P_2=\frac{G(P_1)-1}{1-\eta^2T_3^2}P_1.\tag{32}$$

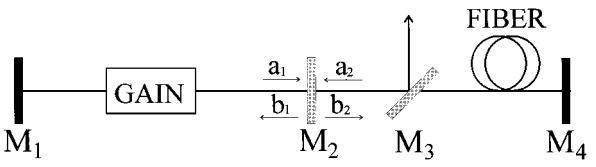

FIG. 8. The Fabry-Pérot configuration. a_i and b_i denote field amplitudes, M_2 is a beam splitter, M_3 the output coupler.

The fixed points of the fields ($p_i^{(n+1)}=p_i^{(n)}=:p_i$) must fulfill [remember that $\varphi=\varphi(|p_2|^2)$ and $g(P_1)=g(|p_1|^2)$]

$$[1-rg(P_1)][\cos(\varphi)+r_2\eta T_3] = T\eta T_3 g(P_1), \tag{33}$$

$$\Rightarrow g(P_1)=\frac{\cos(\varphi)+r_2\eta T_3}{\eta T_3+r_2\cos(\varphi)}. \tag{34}$$

Additionally, the net phase shift per round trip must vanish to provide fixed points of the phase. So the constraint $\varphi_{\rm nl}+\varphi_{\rm stat}=n\pi$, n integer must be fulfilled. However, the static phase is an external parameter, so that generally this condition is not satisfied and no fixed points of the field amplitudes occur. Nevertheless, Eq. (30) can be solved by the solution

$$p_1^{(n)}=\sqrt{P_{f,1}}e^{i(n\kappa+\psi)}, \tag{35}$$

$$p_2^{(n)}=\sqrt{P_{f,2}}e^{in\kappa},$$

which turns out to be stable in numerical experiments. Similar to the above, these solutions rotate in phase at a rate κ with a phase difference ψ. The squares of these expressions provide two fixed-point solutions of Eq. (31), which we call $P_{f,1}$ and $P_{f,2}$. $P_{f,i}$ can be calculated by the balance of gain and loss

$$1=G(P_{f,1})R_{\rm eff}[\varphi(P_{f,2})] = G(P_{f,1})\frac{(r_2-\eta T_3)^2+4r_2\eta T_3\cos^2\frac{\varphi}{2}}{(1-r_2\eta T_3)^2+4r_2\eta T_3\cos^2\frac{\varphi}{2}} \tag{36}$$

and the relation Eq. (32). With $P_{f,1}$ and $P_{f,2}$, κ and ψ can be calculated by

$$e^{i\kappa}-\eta T_3 g e^{i(\varphi-\kappa)}=r_2 g-r_2\eta T_3 e^{i\varphi}. \tag{37}$$

The solution is

$$\tan\frac{\kappa}{2}=\frac{\sqrt{1+2g\eta T_3\cos(\varphi)+G\eta^2T_3^2-R_2\eta^2T_3^2\sin^2(\varphi)}}{\eta T_3(g+r_2)\sin(\varphi)} - \frac{1+g\eta T_3\cos(\varphi)}{\eta T_3(g+r_2)\sin(\varphi)}, \tag{38}$$

$$\cos(\psi)=\frac{T_2P_{f,1}+(R_2-\eta^2T_3^2)P_{f,2}}{2r_2t_2\sqrt{P_{f,1}P_{f,2}}}. \tag{39}$$

The stability of this solution depends on φ and its power dependence via $\varphi_{\rm nl}$, compare Eq. (29)and Eq. (28). $\varphi_{\rm nl}$ at the onset of unstable behavior is shown in Fig. 9 as a function of $\eta^2T_3^2$. This quantity describes the fraction of power returning to the main cavity and at the same time provides a measure for the finesse of the fiber branch. The operational state described by these fixed points is thus stable for very weak nonlinearity; at the first bifurcation it becomes unstable. As expected, the threshold decreases with increasing feedback from the auxiliary resonator, corresponding also to increasing fiber cavity finesse. A comparison with the ''M'' topology shows that for parameters as typically used in experiments, instabilities are much more likely to occur in the ''FP'' configuration. This is reasonable, because one would intuitively assume that multiple-beam interference would be more prone to instability than two-beam interference.

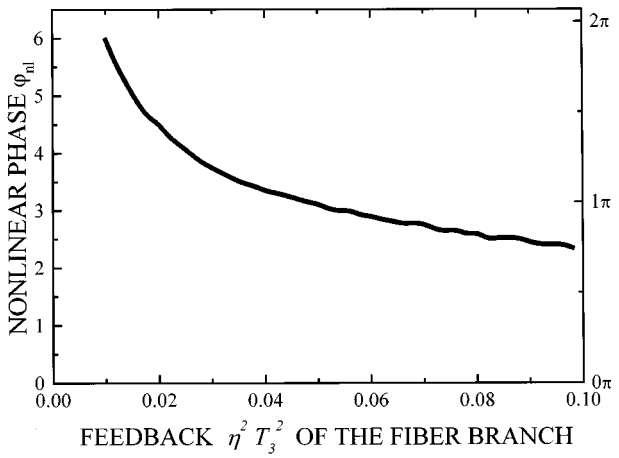

FIG. 9. Nonlinear phase at the onset of instability as a function of the fraction of power $\eta^2T_3^2$ returning from the fiber branch, ''FP'' configuration. Parameters: $R_2<0.8$; $\varphi_{\rm stat}$ and γL were adjusted such that the minimum value of $\varphi_{\rm nl}$ is obtained.

For this topology experiments have been reported about the regime of instability; therefore, we also performed a numerical study of the map at and beyond the threshold of instability. Figure 10 shows the result for some representative set of parameter values. We chose to display a scan of the nonlinearity coefficient $2\gamma L$; while this choice has no immediate experimental counterpart, it shows the influence of the amount of instability most clearly. Figure 10 has three parts: The top panel shows a bifurcation diagram, the second panel a spectrogram obtained from a Fourier transform of the data in the top panel. The bottom panel displays the spectrum of Lyapunov exponents from Eq. (13) obtained by the iteration of Eq. (30). Since Eq. (30) is a two-dimensional complex map, the Jacobian is four-dimensional, and there are four Lyapunov exponents. Note that the broadband in the bifurcation diagram at $2\gamma L=5.3\ldots6$ kW^{-1} (disregarding the periodic window near $2\gamma L=5.6$kW^{-1}) has a corresponding broadband spectrum and a positive Lyapunov exponent and is thus clearly identified as chaotic, whereas a similar band in the bifurcation diagram at $2\gamma L=1.9\ldots3.2$ kW^{-1} has discrete spectral lines and no positive Lyapunov exponent and is thus identified as quasiperiodic.

D. The ''Φ'' configuration

This configuration, resembling the letter ''Φ'' in its shape, is unique in that it has no unused output or input from a beam splitter (see Fig. 11). A laser resonator contains a beam splitter M_2 which steers part of the intracavity light towards a fiber; light at the other fiber end returns to the main cavity from the other side of M_2. The fiber subcavity has the same optical length as the main cavity except for the phase bias $\varphi_{\rm stat}$ (see Fig. 11). Note that light propagation through the fiber is bidirectional. Due to this bidirectionality a description requires three coupled maps

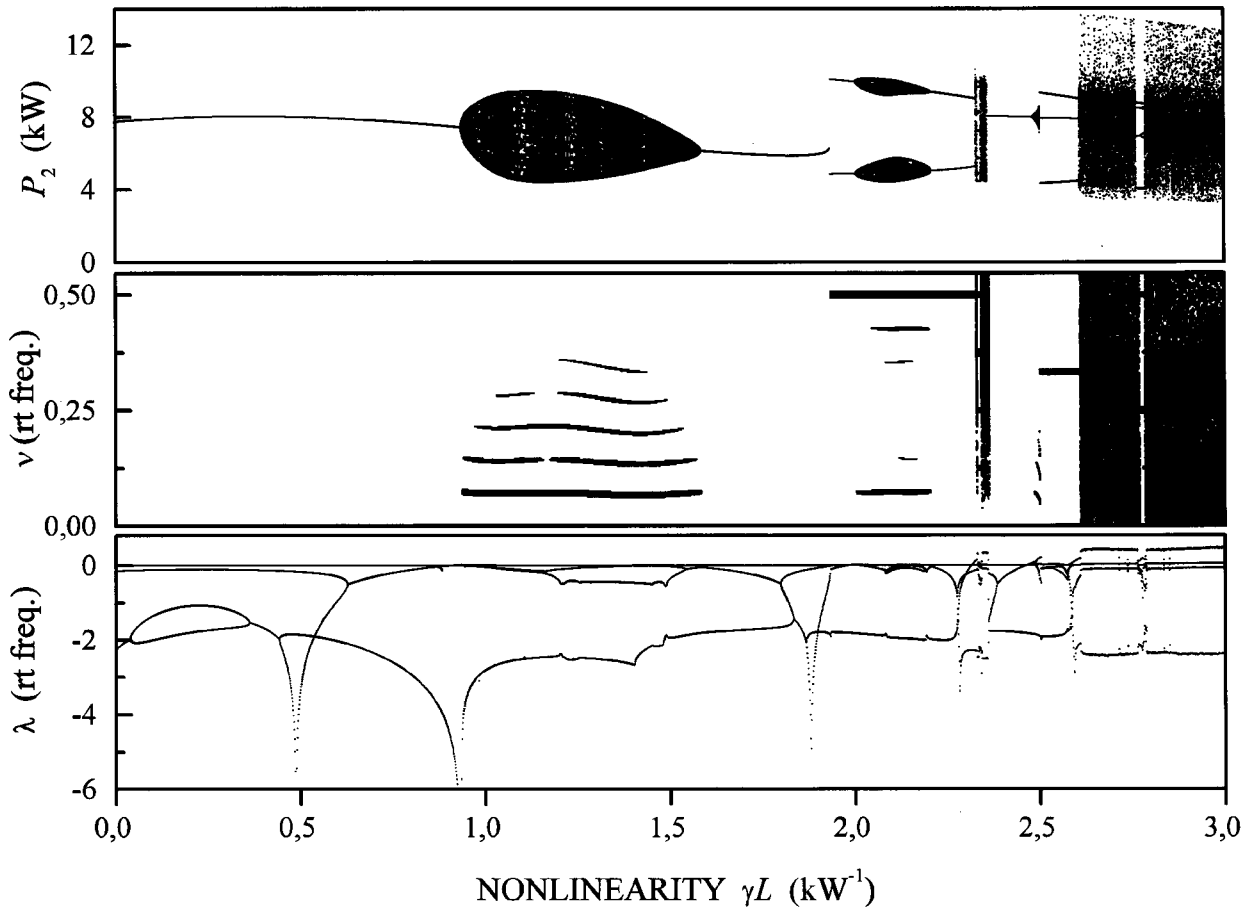

FIG. 10. Route to chaos calculated for the Fabry-Pérot configuration. Parameters: $R_2=0.8$, $\eta^2 T_3^2=0.04$, and $\varphi_{\text{stat}}=-1{,}16$. For each value of γL, 11 000 iterations were calculated. The first 1000 were disregarded to let transients die out. Then, data were plotted in the following way: Top: Bifurcation diagram (power in fiber arm P_2 vs nonlinearity coefficient γL). The next 50 iterations are plotted. Middle: Spectrogram, frequencies ν for which the power density exceeds a threshold. Fourier transforms of 512 iterations of P_2 are used. Threshold was chosen at 40 dB below the maximum power occurring at this γL; in the chaotic regime threshold was increased to limit the number of points. Bottom: Lyapunov spectrum, calculated using all 10 000 remaining data points ($N_1=10$, $N_2=1000$). Finally, γL was incremented; the last iterates were kept as new initial values to simulate a continuous scan. Note that due to hysteresis effects, different choices of initial conditions, e.g., a downward scan, would result in a somewhat different picture.

$$a_4^{(n+1)}=[t_2 a_4^{(n)}-r_2 g(b_1) b_1^{(n)}]\,\eta e^{i\varphi_{\text{cw}}}, \tag{40}$$

$$b_1^{(n+1)}=t_2 r_3[r_2 a_4^{(n)}+t_2 g(b_1) b_1^{(n)}]-r_2 b_4^{(n)}\,\eta e^{i\varphi_{\text{ccw}}},$$

$$b_4^{(n+1)}=r_2 r_3[r_2 a_4^{(n)}+t_2 g(b_1) b_1^{(n)}]+t_2 b_4^{(n)}\,\eta e^{i\varphi_{\text{ccw}}}.$$

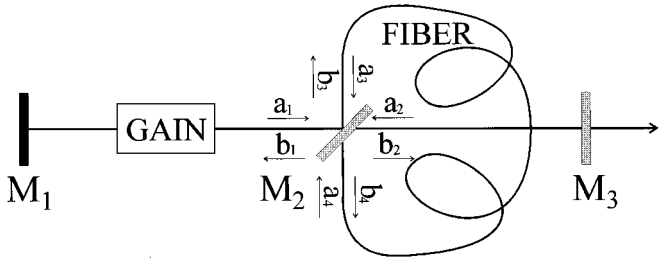

FIG. 11. The ''Φ'' configuration. a_i, b_i denote field amplitudes; M_2 is the beam splitter, and M_3 is the output coupler.

Again, there are two different nonlinear phase shifts for clockwise and counterclockwise propagation through the fiber, respectively

$$\varphi_{\text{cw}}=\gamma L\,\eta|b_3|^2+\varphi_{\text{stat}}, \tag{41}$$

$$\varphi_{\text{ccw}}=\gamma L\,\eta|b_4|^2+\varphi_{\text{stat}}. \tag{42}$$

A system of three coupled equations is much more difficult to treat than the cases described before. Therefore, we have not yet attempted an analytical treatment. From numerical exploration, we can tentatively say that (1) the threshold appears to be low in comparison, and (2) the range of possible types of behavior in the instability regime appears to be much wider—which is not surprising, of course.

V. DISCUSSION

We have shown that the models for four different topologies of APM lasers differ in their degree of complexity. For the much-studied Fabry-Pérot case we also venture into the unstable domain. We find period doubling into chaos and

quasiperiodicity, which were indeed both observed experimentally by Sucha *et al.* [12] and by Morgner, Rolefs, and Mitschke [13]. Quasiperiodicity was explained in [13] as a result of cavity length mismatch; obviously, another mechanism exists in the absence of such mismatch. For a Michelson configuration, the observation of instabilities is unlikely for all reasonable parameter values. For a ''P'' or a Fabry-Pérot configuration, period doubling and chaos should be much more readily observable. This conclusion is confirmed by Sucha, Bolton, and Chemla [16] who reported on a remarkable difference in stability behavior for the Michelson and the Fabry-Pérot case in both numerical simulation and experiment. By the same logic, the dynamical behavior of the ''Φ'' configuration is expected to be even more prone to various kinds of instabilities. Experimental findings reported by Groninga and Harde [17] seem to support this conclusion, but a full experimental verification is presently lacking. Our results suggest that in search for the most stable configuration, further effort on the ''ϕ'' topology is not warranted.

Our treatment apparently describes the relative stability of the various topologies correctly. We pointed out above, however, that the quasi-cw approximation misses important factors of the dynamics. Let us assess the influence of this approximation by way of analogy: For a passive fiber ring resonator it has been shown in detail that dispersion is a major factor in the dynamics of pulses in a resonator, because it represents a coupling between temporal slices [29–31]. Depending on dispersion sign, there may even be optical turbulence [31–33] or a soliton gas [34]. Note, however, that all these shaping processes occur above the first instability threshold. In fact, the quasi-cw treatment by Ikeda and coworkers [18,19] correctly predicts the instability threshold in spite of its simplifications.

Therefore, to determine conditions for the first threshold we chose the same simplified approach in the expectation that coupling mechanisms like dispersion, bandwidth limitation, gain depletion, etc., will not affect the threshold conditions precisely because all these phenomena begin to exert significant influence only *after* destabilization.

CONCLUSION

Different APM cavity topologies have been investigated analytically by a quasicontinuous-wave treatment. Thresholds for dynamical instability were derived, and the overall dynamical complexity categorized. We conclude that the Michelson configuration is the most robust in that it maintains a regular pulse stream except for extreme choices of parameters. This superior stability has also been found empirically; however, it was attributed to technical factors before [14], whereas we have shown that there is a deeper physical root. The other configurations will exhibit dynamical instabilities at parameter values typical for operation. The degree of complexity increases as one passes from the ''P,'' through the ''FP,'' to the ''Φ'' topology. This is in accord with previous observations of such differences in stability. In conclusion, we showed that there can be period doubling and chaos in additive-pulse mode-locked lasers due to the interaction of the gain medium with the Kerr nonlinearity, and that the cavity arrangement plays the crucial role.

ACKNOWLEDGMENTS

Discussions with and assistance from L. Rolefs, R. Hartwigk, and D. Jacob are gratefully acknowledged. We also benefited from fruitful discussions with H. Harde and H. Groninga who shared their expertise on the ''P'' and the ''Φ'' cavity arrangements with us. Financial support from Deutsche Forschungsgemeinschaft is gratefully acknowledged.

[1] X. Zhu, P. N. Kean, and W. Sibbett, IEEE J. Quantum Electron. **25**, 2445 (1989).
[2] L. F. Mollenauer and R. H. Stolen, Opt. Lett. **9**, 13 (1984).
[3] F. M. Mitschke and L. F. Mollenauer, IEEE J. Quantum Electron. **QE-22**, 2242 (1986).
[4] F. Oulette and M. Piché, Opt. Commun. **60**, 99 (1986); Can. J. Phys. **66**, 903 (1988).
[5] M. Morin and M. Piché, Opt. Lett. **14**, 1119 (1989).
[6] H. A. Haus, J. G. Fujimoto, and E. P. Ippen, J. Opt. Soc. Am. B **8**, 2068 (1991).
[7] K. J. Blow and B. P. Nelson, Opt. Lett. **13**, 1026 (1988).
[8] M. Nakazawa, K. Suzuki, and H. A. Haus, Phys. Rev. A **15**, 5193 (1988).
[9] J. Mark, L. Y. Liu, K. L. Hall, H. A. Haus, and E. P. Ippen, Opt. Lett. **14**, 48 (1989).
[10] E. P. Ippen, H. A. Haus, and L. Y. Liu, J. Opt. Soc. Am B **6**, 1736 (1989).
[11] F. Mitschke, G. Steinmeyer, M. Ostermeyer, C. Fallnich, and H. Welling, Appl. Phys. B **56**, 335 (1993).
[12] G. Sucha, S. R. Bolton, S. Weiss, and D. S. Chemla, Opt. Lett. **20**, 1794 (1995).
[13] U. Morgner, L. Rolefs, and F. Mitschke, Opt. Lett. **21**, 1265 (1996).
[14] R. S. Grant and W. Sibbett, Opt. Commun. **86**, 177 (1991).
[15] D. E. Spence and W. Sibbett, J. Opt. Soc. Am. B **8**, 2053 (1991).
[16] G. Sucha, S. R. Bolton, and D. S. Chemla, *Digest of Conference on Lasers and Electro-Optics* (Optical Society of America, Washington, DC, 1994), paper CThI16, p. 329.
[17] H. Groninga and H. Harde, Verhandl. DPG (VI) **31**, 284 (1996), Q 36.6; *Digest of Conference on Lasers and Electro-Optics Europe (CLEO-Europe)* (Optical Society of America, Washington, DC, 1996), paper CWA4, p. 148.
[18] K. Ikeda, Opt. Commun. **30**, 257 (1979).
[19] K. Ikeda, H. Daido, and O. Akimoto, Phys. Rev. Lett. **45**, 709 (1980).
[20] H. Nakatsuka, S. Asaka, H. Itoh, K. Ikeda, and M. Matsuoka, Phys. Rev. Lett. **50**, 109 (1983).
[21] A. Ankiewicz and C. Pask, J. Austr. Math. Soc. Ser. B **29**, 1 (1987).
[22] See, e.g., W. Koechner, *Solid State Laser Engineering* (Springer, New York, 1996).

[23] K. J. Weingarten, B. Braun, and U. Keller, Opt. Lett. **19**, 1140 (1994).
[24] See, e.g., H. A. Haus, *Waves and Fields in Optoelectronics* (Prentice-Hall, Englewood Cliffs, NJ, 1984).
[25] See, e.g., G. P. Agrawal, *Nonlinear Fiber Optics* (Academic, Boston, 1995).
[26] See, e.g., P. Bergé, Y. Pomeau, and C. Vidal, *Order Within Chaos* (Hermann, Paris, 1984).
[27] E. Ott, Rev. Mod. Phys. **53**, 655 (1981).
[28] H. A. Haus, E. P. Ippen, and K. Tamura, IEEE J. Quantum Electron. **30**, 200 (1994).
[29] G. Steinmeyer, A. Buchholz, M. Hänsel, M. Heuer, A. Schwache, and F. Mitschke, Phys. Rev. A **52**, 830 (1995).
[30] G. Steinmeyer, D. Jaspert, and F. Mitschke, Opt. Commun. **104**, 379 (1994).
[31] G. Steinmeyer, A. Schwache, and F. Mitschke, Phys. Rev. E **53**, 5399 (1996).
[32] G. Steinmeyer and F. Mitschke, Appl. Phys. B **62**, 367 (1996).
[33] F. Mitschke, G. Steinmeyer, and A. Schwache, Physica D **96**, 251 (1996).
[34] F. Mitschke, A. Schwache, U. Morgner, and G. Steinmeyer, *International Quantum Electronics Conference* (Optical Society of America, Washington, DC, 1996), paper WL69, p. 170.